

Article

Deep Structure of Epithermal Deposits in Youxi Area: Insights from CSAMT and Dual-Frequency IP Data

Huanyin He ¹, Jinrong Wang ¹, Wu Wen ¹, Rencong Tian ¹, Jiansui Lin ¹, Weiqiang Huang ¹ and Yabin Li ^{2,*}

¹ The Second Geological Exploration Institute of China Metallurgical Geology Bureau, Fuzhou 350108, China; ringsliver@163.com (H.H.); zgbjrongw@163.com (J.W.); dudugoldfish2018@163.com (J.L.)

² College of Geoexploration Science and Technology, Jilin University, Changchun 130026, China

* Correspondence: yabinli18@gmail.com

Abstract: Epithermal deposits represent a significant category of gold occurrences, with their subsurface structure playing a key role in reserve assessments. Fujian Province, characterized by extensive Mesozoic volcanic activities, stands out as a noteworthy region for shallow hydrothermal mineralization in China. This paper focus on the Youxi area within Fujian Province, employing the dual-frequency induced polarization method (DFIP) and controlled-source audio-frequency magnetotelluric method (CSAMT) to investigate the target ore. The DFIP results revealed predominant northeast-oriented zones with high polarizability and notable apparent resistivity. The CSAMT data were inverted using the SCS2D software. Two-dimensional resistivity profiles reveal a three-layer electrical structure, comprising subsurface banded rhyolites influenced by fault zones, intermediate-low resistivity sandstone layers, and deep-seated high-resistivity conglomerates. The resistivity gradient zones and highly polarizable locations align closely with known local faults. We interpreted these resistivity gradient zones as prospective target areas for mineralization, a hypothesis subsequently validated by drilling results. Combining geochemical analyses of epithermal gold deposits with the electrical resistivity structure, we propose an explanatory model for the mechanism of the formation of epithermal gold–silver deposits in the Youxi area. The magmatic hydrothermal fluids ascended along the fault, underwent convection-driven interaction with meteoric waters, and subsequently metasomatized the host rocks. This integrated approach provides valuable insights into the geological processes governing epithermal gold–silver deposit formation in the Youxi region.

Keywords: dual-frequency induced polarization method; controlled-source audio-frequency magnetotelluric method; epithermal deposits



Citation: He, H.; Wang, J.; Wen, W.; Tian, R.; Lin, J.; Huang, W.; Li, Y. Deep Structure of Epithermal Deposits in Youxi Area: Insights from CSAMT and Dual-Frequency IP Data. *Minerals* **2024**, *14*, 27. <https://doi.org/10.3390/min14010027>

Academic Editors: Ahmed Mohammed Eldosouky, Stephen Eguba Ekwok and Stanislaw Mazur

Received: 4 November 2023

Revised: 11 December 2023

Accepted: 20 December 2023

Published: 25 December 2023



Copyright: © 2023 by the authors. Licensee MDPI, Basel, Switzerland. This article is an open access article distributed under the terms and conditions of the Creative Commons Attribution (CC BY) license (<https://creativecommons.org/licenses/by/4.0/>).

1. Introduction

Epithermal deposits are typically characterized by low temperatures (<300 °C), low salinity (<10 wt.% NaCl), and relatively shallow depths (~1–2 km) [1] and form one of the most important types of gold–silver mineralization in the world [2]. The formation of these deposits, often closely associated with volcanic activity, occur in various tectonic settings, including island arcs, continental arcs, and back-arc extension environments [3].

Since the Late Proterozoic, southeast China has experienced extensive volcanic activity, especially in the Late Jurassic and Early Cretaceous [4], during which widespread epithermal ore deposits formed, making it one of China’s most important gold–silver mining areas [5]. Fujian province hosts a broad distribution of Mesozoic continental volcanoes and numerous epithermal deposits are found across the entire province. Some notable regions include Shanghang in the southwest, Jianning in the northwest, Zhenghe-Jian’ou in the north, and Dehua-Youxi-Yongtai in the central-eastern part of the province, all of which have yielded large polymetallic deposits [6–8]. The Dehua-Youxi-Yongtai region is commonly referred to as the “Golden Triangle” exploration area, where significant gold mines, such as Ancun, Qiucun, and Shuangqishan, have been discovered [9–12]. Several scholars

have conducted research using geological chronology, fluid inclusion data, and isotope dating, and concluded that the metals in this area originate from magmatic hydrothermal sources [13–15]. The precipitation of gold is believed to result from the evolution of magmatic fluids mixing with meteoric water, which plays a significant role in mineralization stage, categorizing these deposits as shallow epithermal ore deposits [6,7,16].

The study area of this research is located in the southeast of Youxi County. Since the 1990s, informal mining teams have been engaged in the extraction of gold deposits in this region. During field geological surveys, exposed gold veins have been discovered, and geochemical investigations have revealed significant geochemical anomalies in the area. However, the lack of geophysical data has limited the delineation of mineralization target zones within the research area.

During the epithermal mineralization, the interaction between minerals, heat sources, and fluids serves as the fundamental basis for mineral formation [17]. As magmatic hydrothermal fluids migrate from the deep to the Earth's surface, they interact with the mineral source (host rocks) and fluids within the strata, leading to the creation of alteration minerals [18]. Typically, gold–silver mineralization is commonly linked with vein quartz or disseminated sulfides, resulting in noticeable variations in electrical resistivity between the hydrothermal fluids, alteration minerals, and host rocks [19]. Furthermore, highly permeable fractured fault zones and fissures often serve as conduits for the ascent of deep-seated hydrothermal fluids [20], frequently resulting in the dispersion of alteration minerals along fault zones. The differences in electrical properties between alteration minerals and fault zones, as well as host rocks, make it feasible to detect epithermal ore deposits using electromagnetic methods.

Electromagnetic methods have been extensively employed in the exploration of ore deposits, including rare earth mineral exploration [21], as well as the exploration of copper–nickel deposits [22], lead–zinc ore deposits [23], and gold deposits [24]. These research endeavors have effectively demonstrated the potential applications of electromagnetic techniques in mineral exploration. Particularly noteworthy is the controlled-source audio-frequency magnetotelluric method (CSAMT), which offers advantages such as greater exploration depth and a wider range of parameters compared to conventional electrical methods. CSAMT, employing artificial sources, exhibits high signal-to-noise ratios and efficient data acquisition, making it a widely utilized tool for the exploration of ore deposits [25–27].

In this study, both dual-frequency induced polarization (DFIP) and CSAMT were utilized. The dual-frequency induced polarization method was employed to identify the shallow mineralization target zones within the research area. Subsequently, the controlled-source audio-frequency magnetotelluric method was used to acquire information regarding the deep electrical structure of the study area. By integrating these data with drilling information, the mineralization target areas were delineated. Furthermore, in combination with geological strata information, the study delved into the shallow hydrothermal transport pathways and analyzed the mineralization mechanisms within the target region.

2. Geological Settings

Fujian volcanic depression belt was formed on the basis of the Himalayan–Indosinian and Caledonian periods and underwent large-scale faulting and depression during the Yanshanian Movement [4]. The area is situated in the central segment of the east and sandwiched between the Zhenghe-Dapu fault zone and the Fu'an-Nanjing fault zone (Figure 1a), with the Pu'cheng-Youxi fault zone traversing the study area [28]. Since the Proterozoic era, the region has suffered extensive tectonic–magmatic–mineralization process with close associations between different geological stages and the tectonic settings relevant to mineralization [4]. The research area hosts quartz diorites from the Himalayan–Indosinian period and shallow intrusive rocks and subvolcanic rocks from the Yanshanian period. The tectonic and magmatic events during the Yanshanian period led to extensive

intrusion activity, providing the region with abundant mineral resources, heat sources, and ore-forming spaces, thereby contributing to the formation of rich mineral deposits [9,10,29].

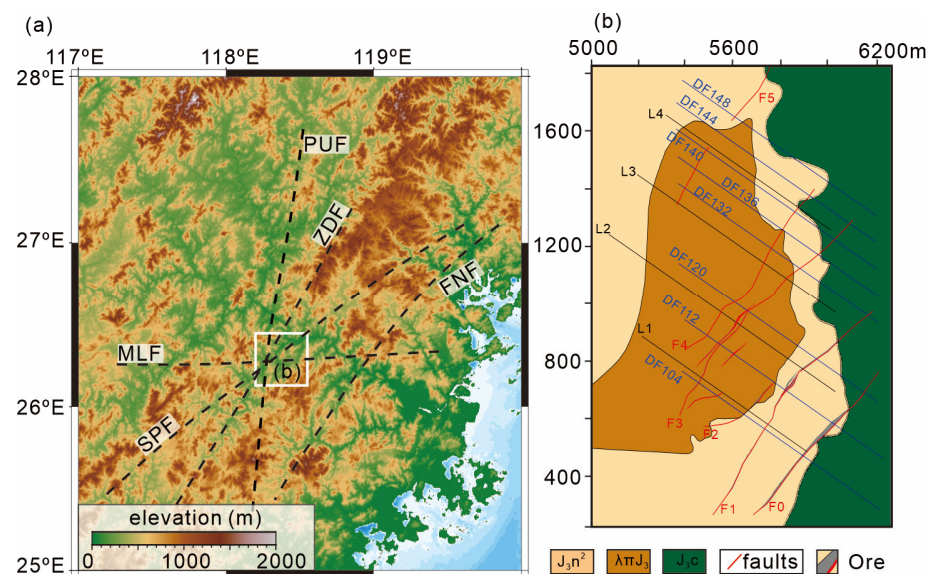


Figure 1. Geological context. (a) Location of the study area in southeast China. (b) Geophysical survey lines in study area. PUF: Pucheng–Youxi fault; ZDF: Zhenghe–Dapu fault; SPF: Shanghang–Pingnan fault; MLF: Mingxi–Luoyuan fault; FNF: Fu’an–Nanjing fault. Solid black and blue lines in (b) represent the observation lines of the CSAMT and DFIP, respectively.

Since the Hercynian–Indosinian period, the study area has witnessed the sequential development of sets of fault structures, including east–west and northeast–southwest striking directions (Figure 1a). Many copper–gold (silver) deposits or occurrences are commonly located at the intersection zone of the NE–SW striking faults. These fault intersections serve as significant controls in ore-guiding and ore-hosting structures. NE and NNE striking fault zones and WE striking faults have undergone compressional and extensional processes and are considered important ore-controlling structures within the study area. These structures influence magma activity, fluid pathways, and ore deposit distribution in the region [6,14,30].

The primary outcropped geological formations are the Late Jurassic Changling Formation (J_3c) and the second segment of the Late Jurassic Nanyuan Formation (J_3n^2) (Figure 1b). The Changling Formation comprises a set of continental volcanic–clastic sediments, including tuffaceous sandstone, siltstones, mudstones, pebbly sandstones, and sandy conglomerates. The second segment of the Nanyuan Formation mainly consists of rhyolitic crystal clast tuff and clastic crystal clast tuff [4]. These volcanic rocks unconformably overlies the Changling Formation. The area also contains intrusive igneous rocks, including rhyolite porphyry, granite porphyry, and olivine basalt. The rhyolite porphyry is primarily distributed along faults and fractures with outcropped in banded or tabular distribution. The porphyry intruding into the Changling Formation occurred prior to the mineralization process and was influenced by later mineralization-related structures, with gold–silver mineralization commonly occurring in the contact zones. The spatial distribution in this region reveals a close relationship between the Changling Formation and Nanyuan Formation and gold–silver mineralization, thus classifying them as important host rocks for mineralization in the region [28].

3. Methodology and Data

The electrical difference between the host rock and the ore is fundamental to conduct the exploration. The electrical resistivity and apparent amplitude frequencies of the host rock, including sandstone, tuff, and rhyolite porphyry, were measured by SQ-5 with

$AB/2 = 6$ m and $MN/2 = 0.5$ m. The host rocks have high resistivity values, ranging from 1000 to 3000 $\Omega\cdot\text{m}$, and low polarization with apparent amplitude frequencies less than 2%. The electrical parameters of the ore deposits are related to the degree of mineralization and exhibit obvious high polarization characteristics in the study area. The significant electrical difference between ore deposits and host rocks favors the geophysical exploration.

3.1. Methodology

3.1.1. Dual-Frequency Induced Polarization Method

The induced polarization (IP) method is a geophysical technique for mineral exploration based on the electrical difference between the host rocks and minerals. It involves observing the electrical potential difference of subsurface mediums during the charging and discharging processes. Based on the method, DFIP was developed, which combines two frequency square-wave currents to simultaneously apply a dual-frequency composite current to the subsurface [31]. This allows for the measurement of potential differences on the surface arising from the induced polarization field containing two principal frequencies. The DFIP is lightweight, highly efficient, and offers high precision. It has found extensive application in China in the fields of mineral resource exploration [32]. Using DFIP to simultaneously obtain low-frequency potential differences ($\Delta V(f_L)$) and high-frequency potential differences ($\Delta V(f_H)$), one can derive the apparent amplitude frequency (F_s) used to characterize the induced polarization effect. F_s is defined as follows:

$$F_s(\%) = \frac{\Delta V(f_L) - \Delta V(f_H)}{\Delta V(f_L)} \times 100\%$$

where the apparent amplitude frequency F_s refers to the percentage change in the amplitude of the induced polarization total field potential difference due to different frequencies, which is related to the properties of the underground medium and the selection of frequencies (f_L and f_H).

3.1.2. Controlled-Source Audio-Frequency Magnetotelluric Method

The CSAMT is developed from the audio-frequency magnetotelluric method. Artificial long-wire sources are deployed on the Earth's surface to serve as a transmitter injecting current as the sources. Numerous observation sites are located far away from the transmitter source and measuring both orthogonal horizontal electric fields and magnetic fields, which results in the determination of the subsurface medium's apparent resistivity and phase. Typically, CSAMT measurements collect scalar data, which includes the E_x electric field component, collected along the survey line, and the magnetic field component H_y , perpendicular to the survey line. According to the definition of plane wave impedance, the resistivity can be described using the following formula based on the definition of plane wave impedance:

$$\rho = \frac{1}{\mu_0 \omega} \left| \frac{E_x}{H_y} \right|^2$$

where μ_0 represents the vacuum permeability and ω denotes the angular frequency. We can derive the commonly used formula for apparent resistivity in CSAMT:

$$\rho_s = 0.2T \left| \frac{E_x}{H_y} \right|^2 = \frac{1}{5f} \left| \frac{E_x}{H_y} \right|^2$$

Based on the skin depth, different frequencies exhibit varying exploration depths when propagating through a subsurface medium. By changing the transmission frequency, the observed signal can be an overall response to the resistivity of subsurface rock at different depths.

3.2. Data Acquisition and Process

3.2.1. DFIP Data

The dual-frequency induced polarization data were collected using the SQ-5 dual-frequency induced polarization instrument from Geosun Hi-technology Co., Ltd. (Changsha, China). Two working frequencies were selected: 4 Hz and 4/13 Hz. The working configure is shown in Figure 2b, with a setup including transmitter electrode separations of $AB = 1200$ m and $MN = 40$ m. A total of 8 survey lines were arranged. During the collection process, we first measured half of the data sites, and then move the transmitter position from AB to $A'B'$ to conduct measurements for the remaining half of the data sites (Figure 2b).

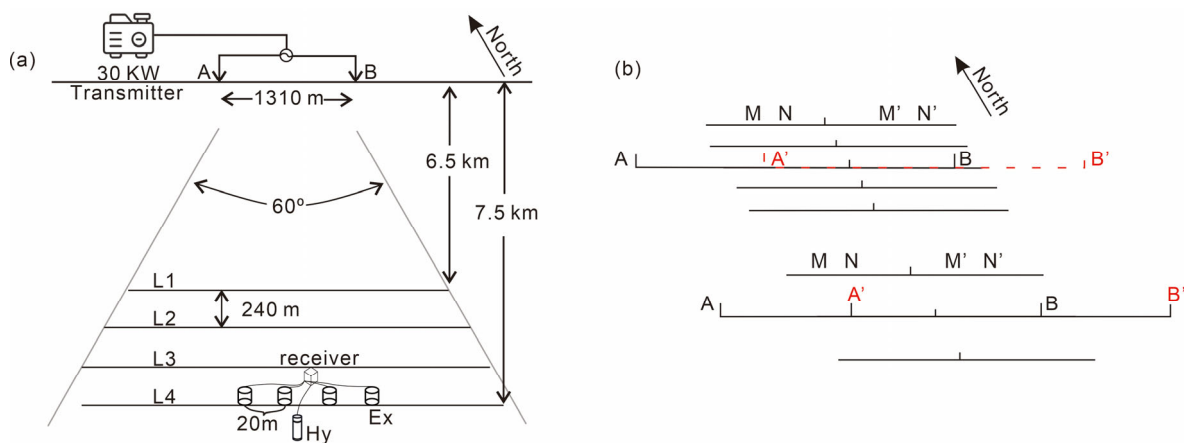


Figure 2. Working configuration in study area. (a) CSAMT configuration. (b) DFIP configuration.

To ensure optimal grounding condition, the transmitter electrodes are located in thick and moist soil. Additionally, the transmitter electrodes were arranged in a circular configuration with a diameter of 1 m, and a saltwater solution was applied to reduce ground resistance, improving the contact conditions between the electrodes and the Earth. After implementing these measures to ensure adequate power supply for the dual frequency induced polarization, data were collected to obtain information on apparent polarizability and apparent resistivity that covered the study area.

3.2.2. CSAMT Data

The CSAMT data for this study were collected using Zonge's GDP-32II multifunction receiver with a 30 kW transmitter. The study area is located at a mountainous region with some exposed rock surfaces. To ensure high-quality data collection, the transmitters sites were carefully selected based on field work, with a total transmitter length of 1310 m. We adopted a series of methods to reduce the grounding resistivity, such as burying aluminum plates, galvanized pipes, and irrigating salt water to ensure good grounding conditions and maintain stable output current.

Four survey lines were deployed parallel to the transmitter source, with source–receiver distances ranging from 6.5 km to approximately 7.5 km. These lines had a line spacing of 240 m and site spacing of 20 m (Figure 2a), resulting in a total of 228 measurement sites. Nonpolarized electrodes were used to collect the electric field signals along the lines (Ex). Magnetic field signals perpendicular to the survey lines (Hy) were also collected. During the collection, the transmitter sequentially emitted current signals with a base of 2, ranging from 1 to 8192 Hz. In each line, several sites are measured twice and calculated the mean square error of the Cagniard resistivity. The relatively small mean square error ($< \pm 5\%$) indicates the acquired data are of good quality.

Considering potential interference from anthropogenic electromagnetic signals, as well as static and source effects, we removed the distorted data sites and conducted the static corrections. The collected data were divided into near-field, transition zone, and far-field

regions. Frequencies less than 256 Hz were seriously disturbed due to the near-field source interference. Thus, these frequencies were cutoff and only data in the range of 256 Hz to 8192 Hz were utilized for the inversion process.

The 2D inversions were conducted using SCS2D software with 2D Occam algorithm. The Occam inversion is a smooth-model-constrained inversion method [33]. While fitting the observed data, it ensures the smooth continuity of the model and selects the smoothest model as the inversion result, greatly enhancing the stability of the inversion process. We performed two-dimensional inversion on the data from the four CSAMT profiles. The initial model was a homogeneous space with resistivity of 100 Ω.m. The elevations of each site were also acquired. Thus, the tomography information was also incorporated into the 2D inversion.

4. Results and Discussion

4.1. Results of the DFIP

Based on the original DFIP data, the entire data covering the study area are visualized with the apparent frequency amplitude and resistivity (Figure 3). The horizontal frequency amplitude and apparent resistivity slices reveal band-like anomalies with a NE striking. These anomalies are interpreted as fault zones. Some faults are consistent with the local faults, while others are newly identified (DF3). The fault zones exhibit significant high polarizability, and the anomalies can be segregated into three distinct areas, identified as A1, A2, and A3.

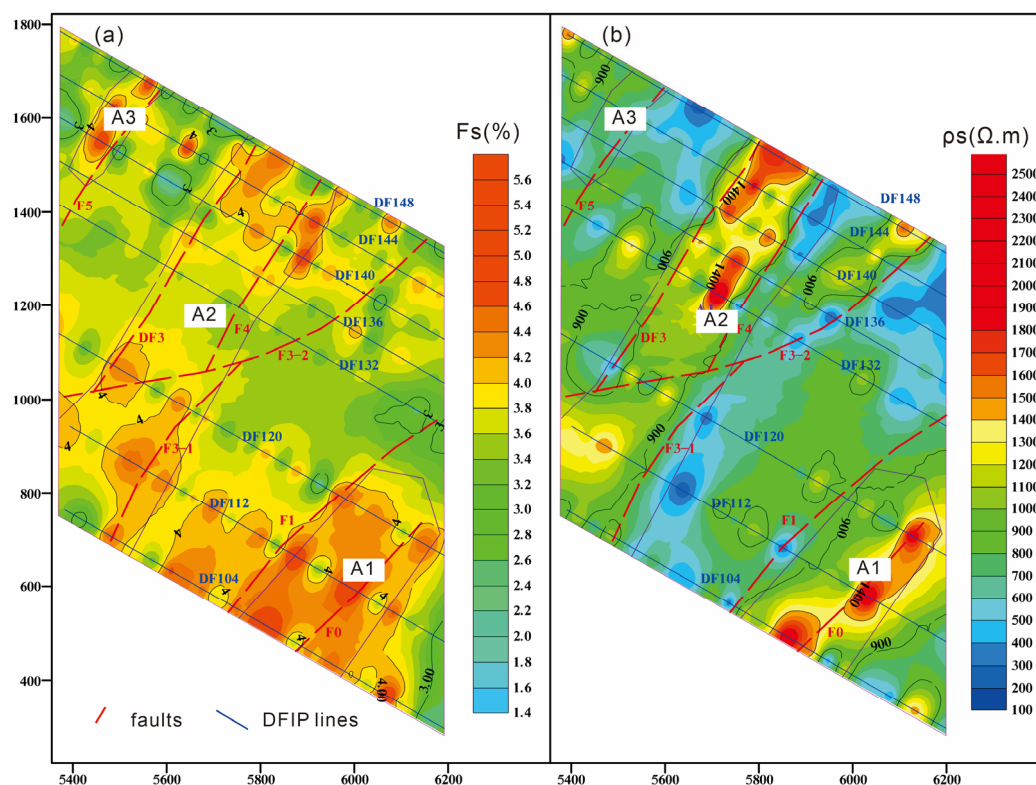


Figure 3. Horizontal results of the DFIP. (a) The apparent amplitude frequency of DFIP data; (b) the apparent resistivity of DFIP.

A1 anomaly is located at the SE part of the study area. This anomaly has a banded-like apparent resistivity distribution and planar-shaped amplitude frequency distribution. The total anomaly has amplitude frequency value exceeding 4.2%. The banded-like resistivity anomaly of A1 has a sharp resistivity value contrast, providing an ideal location for the alteration and mineralization. A2 is in the central part of the study area between the F3 and DF3 faults, with the amplitude frequency exceeding 4%. This anomaly significantly exceeds

the 3% amplitude frequency value rate of the host rock. Meanwhile, apparent resistivity of A1 has a sharp changing from value of approximately 1400 $\Omega\cdot\text{m}$ to about 400 $\Omega\cdot\text{m}$. A3 is situated in the northwest section, to the north of the F5 fault. This anomaly exhibits a distribution trending toward the northeast. The amplitude frequency value within this anomaly exceeds 4%, and it displays relatively high resistivity values in excess of 800 $\Omega\cdot\text{m}$, indicative of a high-resistivity and highly polarizable nature. The three anomalous areas are considered favorable for mineralization.

4.2. Resistivity Characteristics of the CSAMT

The resistivity profiles obtained from the two-dimensional inversion of L1 to L4 are depicted in Figure 4. Based on the resistivity characteristics, the profiles can be roughly divided into three layers: a high resistivity layer split by low resistivity zones, a medium-low resistivity layer, and a deep medium-high resistivity layer. The first layer, namely the high resistivity layer split by low resistivity zones, exhibits significant lateral changes in the shallow profile. The low resistivity zone on the subsurface is speculated to be Quaternary sediments distributed along the terrain, while the low resistivity zone with a large extension depth is interpreted as fault zones. The presence of pore water in this layer may be responsible for the observed near-surface low-resistivity anomaly.

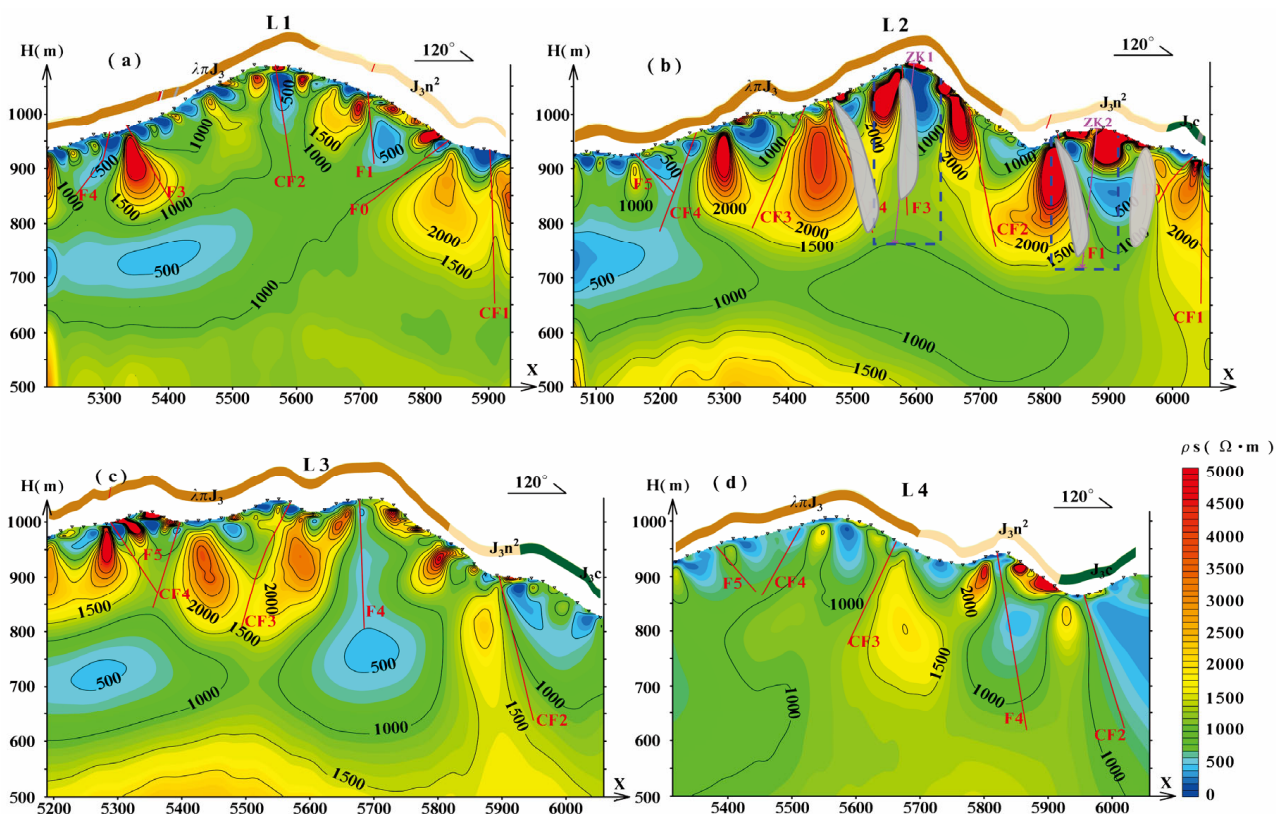


Figure 4. The resistivity results of the CSAMT profile. (a) L1, (b) L2, (c) L3, (d) L4. Redlines in figures represent the faults. The layered color blocks varying with the terrain indicates the outcropped strata. ZK represents the drilling boreholes. Gray shadows in (b) are parts of the ore targets. ZK1 and ZK2 in (b) represent the drilling. Dashed lines in (b) are the section in Figure 5.

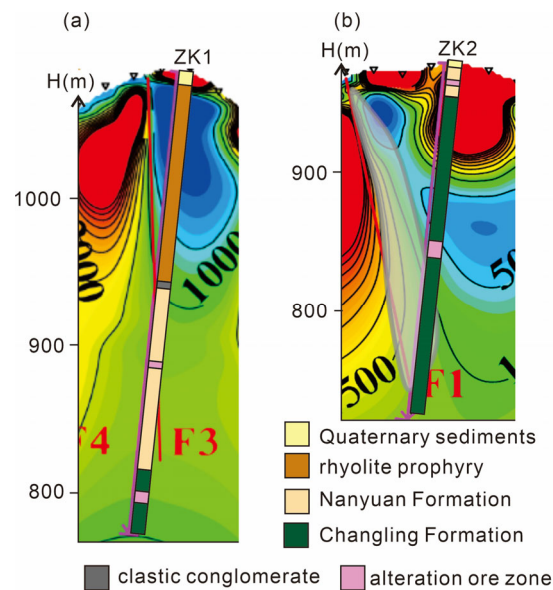


Figure 5. Lithology in the drilling. (a) ZK1. (b) ZK2. The positions of the drilling are in Figure 4b.

The first layer in L1 and L2 profiles becomes thinner with increasing distance, while the L3 profile exhibits a feature of thicker in the middle and thinner on both sides. Based on the stratigraphic sequence and contact relationships, it is evident that the high resistivity layer split by low resistivity zones is predominantly located within the rhyolite, with a smaller portion found in the Nanyuan Formation. The variations in resistivity to some extent reflect the contact relationship between the rhyolite and J_3n^2 . However, due to the characteristics of the EM methods, the actual depth of the rhyolite and J_3n^2 may be shallower than the extended depth of the high-resistivity anomaly revealed, which has also been revealed by the drilling (Figure 5). The high resistivity layers split by low resistivity zones exhibits distinct lateral segmentation, separated by electrical gradient zones. These electrical gradient zones correspond to known fault structures and also reveal some newly discovered faults identified through CSAMT. Fractured faults, hydrothermal alterations, and lithological interfaces can all lead to resistivity anomalies [34–36], resulting in electrical gradient zones. Previous studies on nearby epithermal deposits have indicated that the Nanyuan Formation and rhyolite are the sources of mineralization, with deposition resulting from the interaction between magmatic hydrothermal fluids and meteoric water [37]. This area is characterized as a typical structurally fracture-altered rock-type deposit, with its occurrence strictly controlled by fault structures and influenced by hydrothermal activity [7,17,29]. Therefore, our research focuses on the low resistivity fault zones as potential pathways for the migration of hydrothermal fluids and the high resistivity gradient zones.

Beneath high resistivity layers split by low resistivity zones lies a moderate resistivity layer (100~1000 $\Omega.m$), with depths ranging approximately from 150 to 300 m. This moderate resistivity layer is observed across all four profiles and exhibits a generally horizontal distribution. We infer it to be sandstone of the Nanyuan Formation, consistent with actual drilling results. However, although the lithology of this layer is consistent with that of the outcropped Nanyuan Formation, there is a significant difference in resistivity, which may be attributed to variations in the rock's integrity. In the long-distance points of L1 to L3, this layer has a “dipping” shape, indicating a possible extension into the depth. The deeper, high resistivity layer is presumed to be conglomerate, which presents a marked contrast with the “dipping” sandstone layer.

Based on the electrical gradient zones and the distribution of regional geological structures, we distinguished the fault structures (Figure 4). F0–F5 are consistent with the regional geological structure map, while the others are newly discovered fault zones. The location of some newly discovered fault zones is consistent with the apparent resistivity gradient zone discovered by DFIP. Additionally, the locations of these anomalies are

consistent with the high amplitude abnormal area of DFIP, and corresponds to the surface ore body, further indicating the important role of fault zones in the mineralization process. Based on the location of exposed mineral deposits on the surface and the inversion results of CSAMT, some target areas of mineral deposits in the study area were delineated (Figure 4). Further drilling results also verified the effectiveness of using CSAMT for mineral deposit exploration (Figure 5).

4.3. Formation Mechanism of Mineral Deposits

By a combination the DFIP and CSAMT, we studied the electrical structure of the study area from shallow to deep layers to identify potential ore target in the Youxi area. The lithology in the drilling confirms the results. Further analysis of the formation mechanism of the deposit will provide support for further work. The ore-forming structure in the study area controls the mineralization and crosses through all layers, indicating that the mineralization era was later than the formation era of the host rock. These rocks such as rhyolite, Changlin, and Nanyuan Formations provide ore-forming materials, but the sources of heat sources and ore-bearing fluids are still unclear.

Epithermal deposits typically include magmatic fluids, deep-circulated meteoric waters, and shallow meteoric waters [38]. Geochemical research results from multiple gold deposits located in the “Dehua Youxi Yongtai gold mineralization belt” indicate that the formation of the deposits is related to the mixing of magmatic hydrothermal fluids and diluted precipitation, and meteoric waters plays an important role in the mineralization [6,8,14]. Therefore, the ore-bearing fluids in the study area may be formed by the mixing of deep magmatic hydrothermal solution and surface water.

As high-permeability weak structural zones, fault zones provide pathways for meteoric water [39]. The electrical gradient zones revealed by the resistivity profile effectively depict potential fault information. Several fault zones, extending to depths of several hundred meters, are present in the study area, which could serve as potential pathways for meteoric water migration. Due to the limitations of the working frequencies of the electromagnetic methods we selected, our study depth remains relatively shallow, preventing the effective resolution of deeper plutons. Migration pathways for magmatic fluids originating from the deep subsurface typically follow the paths of minimal energy consumption [20]. Therefore, the electrical gradient zones in deeper sections likely represent potential pathways for the ascent of hydrothermal fluids in the study area (Figure 6).

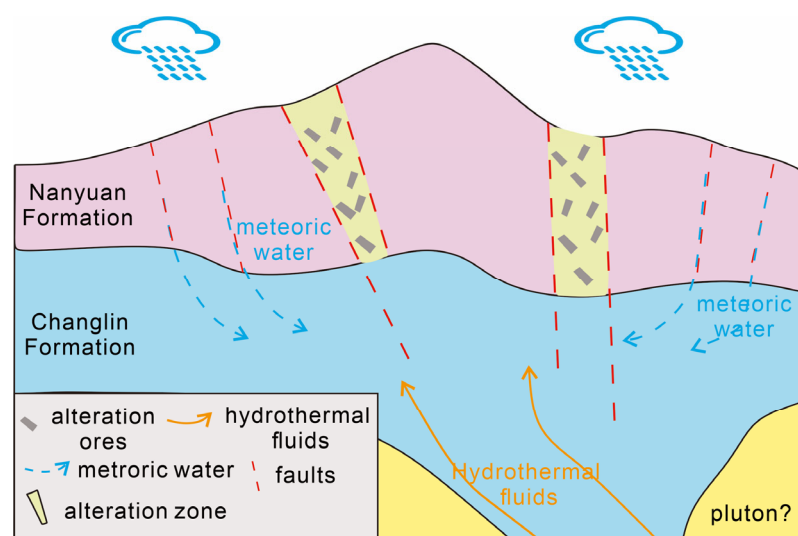


Figure 6. A concept model of epithermal mineralization at the study area based on CSAMT.

By combining the resistivity images from the resistivity profiles with the distribution of deposits, we speculate that the low-resistivity anomaly (F1–F3) extending deeper in

the L2 profile could be the pathway for the ascent of deep-seated hydrothermal fluids. Hydrothermal fluids carrying metallic elements may react with the host rocks, generating alteration minerals that result in the observed moderate resistivity anomalies [19]. The layers at a depth of approximately 600 m are highly permeable and rich in water. Additionally, numerous surface fault zones extend to this layer. Precipitation, groundwater, and magma hydrothermal fluids ascending from the deep subsurface collectively contribute to localized convection. This process further transports ore-forming fluids upward, where they interact with the host rocks, ultimately forming the shallow hydrothermal mineralization area in the area.

5. Conclusions

The outcropped gold–silver ore in the Youxi area make it a potential reserve. We conducted measurements on the ore and host rock and discovered significant characteristics of high resistivity and high apparent frequency amplitude in the ore. To investigate the electrical structure of the area and target mineralization zones, we employed both DFIP and CSAMT. Through the DFIP, three anomalous areas with high resistivity and high apparent frequency amplitude were identified. The 2D resistivity profiles obtained from the CSAMT revealed the presence of numerous shallow subsurface fault zones. By combining the DFIP information with the previously geological information and the surface distribution of mineral deposits, we delineated some target areas in the study area.

To validate the reliability of these target zones, we designed drillings to confirm these anomalies, which revealed a result consistent with the resistivity anomalies from the CSAMT profiles and the polarization anomalies from the DFIP, further confirming the accuracy of the target zones.

The resistivity results also an identified deeper electrical gradient zone extending downward, which are inferred to be pathways for the ascent of magmatic hydrothermal fluids. These fluids carrying the metallic and meteoric waters, resulting in convection in the shallow subsurface, lead to interactions with the host rocks and ultimately form the gold–silver mineral deposits in the study area.

Author Contributions: Conceptualization, H.H. and Y.L.; methodology, H.H., R.T. and J.L.; validation, J.W.; formal analysis, J.W.; investigation, W.W., H.H., J.L. and W.H.; writing—original draft preparation, Y.L.; writing—review and editing, J.W. and Y.L.; visualization, H.H. and Y.L. All authors have read and agreed to the published version of the manuscript.

Funding: This research is funded by the Natural Science Foundation of Fujian Province [2021J01527].

Data Availability Statement: Data are contained within the article.

Acknowledgments: We gratefully acknowledge the Editor and comments and suggestions by two anonymous reviewer that helped us significantly improve the paper.

Conflicts of Interest: The authors declare no conflict of interest.

References

1. Simmons, S.F.; Brown, K.L. Gold in Magmatic Hydrothermal Solutions and the Rapid Formation of a Giant Ore Deposit. *Science* **2006**, *314*, 288–291. [[CrossRef](#)] [[PubMed](#)]
2. Hedenquist, J.W.; Arribas, A.; Gonzalez-Urien, E. *Exploration for Epithermal Gold Deposits*; Reviews in Economic Geology; GeoScienceWorld: McLean, VA, USA, 2000.
3. Zhong, J.; Pirajno, F.; Chen, Y.J. Epithermal Deposits in South China: Geology, Geochemistry, Geochronology and Tectonic Setting. *Gondwana Res.* **2017**, *42*, 193–219. [[CrossRef](#)]
4. Regional Geology of Fujian Province. *Regional Geology of Fujian Province*; Geology Press: Beijing, China, 1985.
5. Mao, J.; Li, X.; White, N.C.; Zhao, C.; Zhang, Z.; Wang, Y.; Hu, H. Types, Characteristics, and Geodynamic Settings of Mesozoic Epithermal Gold Deposits in Eastern China. *Resour. Geol.* **2007**, *57*, 435–454. [[CrossRef](#)]
6. Li, S.N.; Ni, P.; Bao, T.; Li, C.Z.; Xiang, H.L.; Wang, G.G.; Huang, B.; Chi, Z.; Dai, B.Z.; Ding, J.Y. Geology, Fluid Inclusion, and Stable Isotope Systematics of the Dongyang Epithermal Gold Deposit, Fujian Province, Southeast China: Implications for Ore Genesis and Mineral Exploration. *J. Geochemical Explor.* **2018**, *195*, 16–30. [[CrossRef](#)]

7. Li, S.N.; Ni, P.; Bao, T.; Xiang, H.L.; Chi, Z.; Wang, G.G.; Huang, B.; Ding, J.Y.; Dai, B.Z. Genesis of the Ancun Epithermal Gold Deposit, Southeast China: Evidence from Fluid Inclusion and Stable Isotope Data. *J. Geochem. Explor.* **2018**, *195*, 157–177. [[CrossRef](#)]
8. Bao, T.; Ni, P.; Li, S.N.; Xiang, H.L.; Wang, G.G.; Chi, Z.; Li, W.S.; Ding, J.Y.; Dai, B.Z. Geological, Fluid Inclusion, and H–O–C–S–Pb Isotopic Constraints on the Genesis of the Shuangqishan Gold Deposit, Fujian, China. *J. Geochem. Explor.* **2020**, *214*, 106544. [[CrossRef](#)]
9. Niu, S.D.; Guo, J.; Xing, G.F.; Huang, Z.Q.; Wu, H.Y.; Fan, F.P. Magmatism, Geological Setting, Alteration, and Metallogenic Potential of Donghua Area, Dehua County, Fujian Province, Southeast China: Insights from Porphyry Zircon U–Pb and Pyrite Rb–Sr Geochronology, Geochemistry and Remote Sensing. *Ore Geol. Rev.* **2020**, *126*, 103726. [[CrossRef](#)]
10. Xiao, F.; Fan, F.P.; Xing, G.F.; Jiang, S.Y. Late Jurassic Epithermal Mineralization of Shitouban Au Deposit, Dehua–Youxi Area, Southeast China: Quartz Rb–Sr Dating, Fluid Inclusions, and H–O–S–Pb–Sr Isotope Analyses. *J. Geochem. Explor.* **2022**, *236*, 106964. [[CrossRef](#)]
11. Yuan, H.X.; Ni, P.; Chen, H.; Lv, Z.C.; Yu, X.F.; Bao, T.; Wang, G.G.; Hu, R.H.; Du, J.W. Geology, Fluid Inclusion and H–O–S–Pb Isotope Constraint on the Genesis of the Changxing Gold Deposit, Fujian, South China. *Ore Geol. Rev.* **2021**, *129*, 103887. [[CrossRef](#)]
12. Xu, Z.T.; Yang, Q.F.; Sun, J.G.; Lei, F.Z.; Pan, X.D.; Li, Z.W. Origin of Late Jurassic High-K Felsic Volcanic Rocks and Related Au Mineralization in the Dongyang Deposit, Central-Eastern Fujian, SE China, and Its Tectonic Implications. *Geol. J.* **2021**, *56*, 572–598. [[CrossRef](#)]
13. Li, S.G.; Yang, W.; Ke, S.; Meng, X.; Tian, H.; Xu, L.; He, Y.; Huang, J.; Wang, X.C.; Xia, Q.; et al. Deep Carbon Cycles Constrained by a Large-Scale Mantle Mg Isotope Anomaly in Eastern China. *Natl. Sci. Rev.* **2017**, *4*, 111–120. [[CrossRef](#)]
14. Ma, Y.; Jiang, S.Y.; Frimmel, H.E. Metallogeny of the Late Jurassic Qiucun Epithermal Gold Deposit in Southeastern China: Constraints from Geochronology, Fluid Inclusions, and H–O–C–Pb Isotopes. *Ore Geol. Rev.* **2022**, *142*, 104688. [[CrossRef](#)]
15. Zhong, S.; Liu, W.; Zhang, J.; Gan, Q. Origin of Qinxi Silver Polymetallic Deposit in Southeast Coast, China: Evidences from H–O–S–Pb Isotopes and Mineral Rb–Sr Geochronology. *Minerals* **2021**, *11*, 45. [[CrossRef](#)]
16. Rottier, B.; Kouzmanov, K.; Casanova, V.; Bouvier, A.S.; Baumgartner, L.P.; Wälle, M.; Fontboté, L. Tracking Fluid Mixing in Epithermal Deposits—Insights from in-Situ $\delta^{18}\text{O}$ and Trace Element Composition of Hydrothermal Quartz from the Giant Cerro de Pasco Polymetallic Deposit, Peru. *Chem. Geol.* **2021**, *576*, 120277. [[CrossRef](#)]
17. Huang, S.; Chen, Y.; Lin, M.; Li, Q. Mineralization Series and Resource Potential of Subvolcanic-Hydrothermal Au(Ag) Deposites in Central Fujian. *Geol. China* **2005**, *32*, 115–121.
18. Roots, E.A.; Hill, G.J.; Frieman, B.M.; Wannamaker, P.E.; Maris, V.; Calvert, A.J.; Craven, J.A.; Smith, R.S.; Snyder, D.B. Magmatic, Hydrothermal and Ore Element Transfer Processes of the Southeastern Archean Superior Province Implied from Electrical Resistivity Structure. *Gondwana Res.* **2022**, *105*, 84–95. [[CrossRef](#)]
19. Xu, S.; Xu, F.; Hu, X.; Zhu, Q.; Zhao, Y.; Liu, S. Electromagnetic Characterization of Epithermal Gold Deposits: A Case Study from the Tuoniuhe Gold Deposit, Northeast China. *Geophysics* **2020**, *85*, B49–B62. [[CrossRef](#)]
20. Gudmundsson, A. The Propagation Paths of Fluid-Driven Fractures in Layered and Faulted Rocks. *Geol. Mag.* **2022**, *159*, 1978–2001. [[CrossRef](#)]
21. Peacock, J.R.; Denton, K.M.; Ponce, D.A. Three-Dimensional Electrical Resistivity Characterization of Mountain Pass, California and Surrounding Region. *Geochem. Geophys. Geosyst.* **2021**, *22*, e2021GC010029. [[CrossRef](#)]
22. Zhang, J.; Zeng, Z.; Zhao, X.; Li, J.; Zhou, Y.; Gong, M. Deep Mineral Exploration of the Jinchuan Cu–Ni Sulfide Deposit Based on Aeromagnetic, Gravity, and CSAMT Methods. *Minerals* **2020**, *10*, 168. [[CrossRef](#)]
23. Guo, Z.; Hu, L.; Liu, C.; Cao, C.; Liu, J. Application of the CSAMT Method to Pb–Zn Mineral. *Minerals* **2019**, *9*, 2–12. [[CrossRef](#)]
24. Song, M.; Xue, G.; Liu, H.; Li, Y.; He, C.; Wang, H.; Wang, B.; Song, Y.; Li, S. A Geological-geophysical Prospecting Model for Deep-seated Gold Deposits in the Jiaodong Peninsula, China. *Minerals* **2021**, *11*, 1393. [[CrossRef](#)]
25. Hu, X.; Peng, R.; Wu, G.; Wang, W.; Huo, G.; Han, B. Mineral Exploration Using CSAMT Data: Application to Longmen Region Metallogenic Belt, Guangdong Province, China. *Geophysics* **2013**, *78*, B111–B119. [[CrossRef](#)]
26. Chen, J.; Li, Z.; Tian, B.; Chen, X.; Zheng, J.; Zhang, C.; Zhao, W.; Zhang, F. Using the CSAMT Method to Predict Deep Mineralisation of Copper and Molybdenum: A Case Study of the Zhongxingtun Area in Inner Mongolia, China. *Explor. Geophys.* **2020**, *51*, 203–213. [[CrossRef](#)]
27. Lv, H.; Xu, L.; Yang, B.; Su, P.; Xu, H.; Wang, H.; Yao, C.; Su, P. Mineralization Based on CSAMT and SIP Sounding Data: A Case Study on the Hadamengou Gold Deposit in Inner Mongolia. *Minerals* **2022**, *12*, 1404. [[CrossRef](#)]
28. Huang, W.; Hou, H.; Du, Q.; Gao, X.; He, S. Ore Characteristics and Silver Occurrence State of Jihua Silver Deposit in Fujian. *Miner. Resour. Geol.* **2022**, *36*, 542–546.
29. Xiao, F.; Fan, F.P.; Xing, G.F.; Jiang, S.Y. Ore Genesis of Qingyunshan Cu–Au Deposit in the Dehua–Youxi Area of Fujian Province, Southeastern China: Constraints from U–Pb and Re–Os Geochronology, Fluid Inclusions, and H–O–S–Pb Isotope Data. *Ore Geol. Rev.* **2021**, *132*, 104006. [[CrossRef](#)]
30. Xu, N.; Li, S.R.; Wu, C.L.; Santosh, M. Geochemistry and Geochronology of the Dongyang Gold Deposit in Southeast China: Constraints on Ore Genesis. *Geol. J.* **2020**, *55*, 425–438. [[CrossRef](#)]
31. He, J. *Dual-Frequency Induced Polarization Method*; Higher Education Press: Beijing, China, 2006.

32. Liu, J.; He, J.; Zhang, Z.; Huang, J.; Jia, P.; Li, Y. Dual-Frequency Induced Polarization Method and Its Application(in Chinese). *Chin. Geol.* **2001**, *28*, 31–39.
33. Constable, S.C.; Parker, R.L.; Constable, C.G. Occam's Inversion: A Practical Algorithm for Generating Smooth Models from Electromagnetic Sounding Data. *Geophysics* **1987**, *52*, 289–300. [[CrossRef](#)]
34. Samrock, F.; Grayver, A.V.; Eysteinnsson, H.; Saar, M.O. Magnetotelluric Image of Transcrustal Magmatic System Beneath the Tulu Moyo Geothermal Prospect in the Ethiopian Rift. *Geophys. Res. Lett.* **2018**, *45*, 12847–12855. [[CrossRef](#)]
35. Tsukamoto, K.; Aizawa, K.; Chiba, K.; Kanda, W.; Uyeshima, M.; Koyama, T.; Utsugi, M.; Seki, K.; Kishita, T. Three-Dimensional Resistivity Structure of Iwo-Yama Volcano, Kirishima Volcanic Complex, Japan: Relationship to Shallow Seismicity, Surface Uplift, and a Small Phreatic Eruption. *Geophys. Res. Lett.* **2018**, *45*, 12821–12828. [[CrossRef](#)]
36. Hill, G.J.; Bibby, H.M.; Peacock, J.; Wallin, E.L.; Ogawa, Y.; Caricchi, L.; Keys, H.; Bennie, S.L.; Avram, Y. Temporal Magnetotellurics Reveals Mechanics of the 2012 Mount Tongariro, NZ, Eruption. *Geophys. Res. Lett.* **2020**, *47*, e2019GL086429. [[CrossRef](#)]
37. Ni, P.; Pan, J.Y.; Huang, B.; Wang, G.G.; Xiang, H.L.; Yang, Y.L.; Li, S.N.; Bao, T. Geology, Ore-Forming Fluid and Genesis of the Qiucun Gold Deposit: Implication for Mineral Exploration at Dehua Prospecting Region, SE China. *J. Geochem. Explor.* **2018**, *195*, 3–15. [[CrossRef](#)]
38. Hosono, T.; Nakano, T. Pb-Sr Isotopic Evidence for Contribution of Deep Crustal Fluid to the Hishikari Epithermal Gold Deposit, Southwestern Japan. *Earth Planet. Sci. Lett.* **2004**, *222*, 61–69. [[CrossRef](#)]
39. McIntosh, J.C.; Ferguson, G. Deep Meteoric Water Circulation in Earth's Crust. *Geophys. Res. Lett.* **2021**, *48*, e2020GL090461. [[CrossRef](#)]

Disclaimer/Publisher's Note: The statements, opinions and data contained in all publications are solely those of the individual author(s) and contributor(s) and not of MDPI and/or the editor(s). MDPI and/or the editor(s) disclaim responsibility for any injury to people or property resulting from any ideas, methods, instructions or products referred to in the content.